Fuel Cells Bulletin
ISSN: 1464-2859

An Aeromagnetic Compensation Algorithm based on Complete Ensemble Empirical Mode Decomposition with Adaptive Noise and a Physics-Guided Neural Network

Yuan Gao [1,2], Zhijie Qu [1,2], Kang Xing [3,4], Zhenlin Du [1,2], Xiaojuan Zhang [1,2,*]

[1]Aerospace Information Research Institute, Chinese Academy of Sciences, Beijing 100094, China;

[2]School of Electronic, Electrical and Communication Engineering, University of Chinese Academy of Sciences, Beijing 100049, China;

[3]State Key Laboratory of Space-Earth Integrated Information Technology, Beijing 100095, China;

[4]Beijing Institute of Satellite Information Engineering, Beijing 100095, China

[*]Correspondence: xjzhang@aircas.ac.cn

Abstract: Aeromagnetic exploration is a magnetic field exploration method that detects changes in the spatial magnetic field by carrying a magnetometer on an aircraft. However, during the measurement process, the magnetic field data is often interfered by the aircraft's own ferromagnetic materials and maneuvers. The role of aeromagnetic compensation is to eliminate this part of the interference, which is crucial to improving the quality of aeromagnetic exploration data. In this study, we introduce a novel method for aeromagnetic compensation, which is employed to eliminate the interference from aircraft platforms. The proposed method utilizes complete ensemble empirical mode decomposition with adaptive noise (CEEMDAN) to decompose the magnetic field data into multiple feature components. These decomposed features are subsequently input into a physics-guided neural network (PGNN), which was designed to remove magnetic interference from the data. The core idea behind this method is that CEEMDAN effectively decomposes magnetic field data into features that are more easily learned by the neural network. The method leverages both data-driven and model-driven advantages by embedding the Tolles–Lawson (T-L) model into the neural network, thereby compensating for both linear and nonlinear interference. The results of simulation and real experiments show that the proposed method outperforms traditional model-driven and data-driven techniques, especially when the quantity and quality of data are limited.

Keywords: Aeromagnetic compensation; complete ensemble empirical mode decomposition with adaptive noise; physics-guided neural network

1. Introduction

Unmanned aerial vehicle (UAV) aeromagnetic surveys are extensively utilized in geological exploration, military reconnaissance, unexploded ordnance detection, and other fields [1,2] due to their ability to balance detection efficiency with spatial resolution [3]. However, the raw data collected by magnetic survey systems often contain interferences from platforms, equipment, and other sources, in addition to the geomagnetic background field and target anomaly field. Such interference degrades data quality and compromises the accuracy of data interpretation [4]. Therefore, effective aeromagnetic compensation is essential for enhancing the quality of magnetic survey data [5].

Research on aeromagnetic compensation originated in the 1940s, when Tolles introduced the Tolles–Lawson (T-L) model [6]: a foundational method for addressing aeromagnetic interference. The T-L model decomposes the magnetic interference caused by aircraft maneuvers into three components: a constant magnetic field, an induced magnetic field, and an eddy current magnetic field. These components are expressed as a linear equation with 18 coefficients that must be determined [7]. Based on this, Leliak designed a compensation flight test that requires the aircraft to perform strict sinusoidal maneuvers to enhance compensation accuracy [8]. However, the T-L model assumes that the geomagnetic field is constant, the established equation is ill-conditioned, and there is strong multicollinearity between the input features, which leads to a low compensation accuracy to the model [9]. To

address this, Hardwick [10] proposed the ridge regression algorithm as a replacement for the original least squares (LS) method to solve the coefficients. Ridge regression utilizes L2 regularization to mitigate the collinearity problem, thereby improving the numerical stability of the solution. Wu et al. [11] employed principal component analysis to reduce the dimensionality of the input features, which alleviates multicollinearity to some extent. Additionally, partial least squares regression, truncated singular value decomposition [12], and other methods have been used to solve the compensation coefficients of the T-L model, and they have achieved certain results. Zhao et al. [13] discovered that the variables con- tributing to multicollinearity are related to flight direction, and they proposed identifying the flight direction of the aircraft. They then used variance inflation factors to assess the impact of model input features on multicollinearity and eliminated redundant features to enhance the stability of the numerical solution. Building on this, Bi et al. [14] incorporated the T-test to further eliminate less significant variables, thereby reducing the coupling of input features. The aforementioned research on aeromagnetic interference compensation was based on the T-L model, which suffers from several limitations: (1) it assumes that geomagnetic conditions are constant, which may not hold in real-world scenarios; (2) the linear assumption fails to account for complex nonlinear interference from onboard electronic systems [15]; and (3) the strong multicollinearity among input features leads to ill-conditioned equations, thereby reducing compensation accuracy [16].

Neural network methods have increasingly been integrated into aeromagnetic compensation with the advancement of artificial intelligence [17]. These methods aim to leverage the powerful nonlinear mapping capabilities of neural networks to overcome the limitations inherent in the T-L model. The earliest attempt was by Williams [18], who implemented a BP neural network (BPNN), which consists of three sub-networks that are used to predict magnetic field values. The inputs included position, time, and attitude information, while the output comprised the sum of the Earth's background field, time-varying field, and aircraft interference field. Reference [19] introduced an artificial neural network based on a radial basis function using the three components of the fluxgate magnetometer as input features, and they achieved superior compensation performance compared to the BPNN. Reference [20] applied a residual neural network for aeromagnetic interference compensation using the attitude information matrix from the T-L model as the neural network input and residual connections to effectively mitigate the gradient vanishing problem, thereby enhancing the network's stability and trainability. Beyond artificial neural networks, other neural network architectures, such as CNN [21] and LSTM [22], have also been explored in aeromagnetic compensation. Given that the magnetometer and aircraft are not entirely rigidly connected, reference [21] analyzed the nonlinear relationship between tail boom swing displacement and magnetic interference. A 1D CNN was employed for secondary compensation of the T-L model's compensation data, aiming to minimize the impact of aeromagnetic swing noise. However, data-driven methods also face several challenges: (1) they require large datasets for training, which may not be feasible given the high cost of acquiring aeromagnetic flight data; (2) feature selection remains an open issue, as different input features can significantly impact compensation effectiveness; and (3) purely data-driven models lack physical interpretability, making it difficult to validate their reliability in real-world applications. The physics-guided neural network (PGNN) [23] represents one of the latest advances in machine learning. By combining physical models with neural networks, it addresses the limitation of data-driven methods in neural networks. This method uses features derived from physical models as neural network inputs, or it employs physical models to guide the loss functions, thereby enhancing the generalizability, scientific consistency, and interpretability of neural networks. Although this method has shown promising results in engineering fields such as wear prediction [24], power load forecasting [25], and lake temperature modeling, it has yet to be fully explored in aeromagnetic compensation.

To address these limitations, we propose a novel aeromagnetic compensation method that integrates complete ensemble empirical mode decomposition with adaptive noise (CEEMDAN) and PGNN. Our approach is based on the following hypotheses: (1) The CEEMDAN method can effectively decompose the original aeromagnetic signal into meaningful feature components, thereby improving feature selection and enhancing neural network learning [26]; (2) embedding the T-L model into the neural network loss function can provide physical constraints, ensuring the consistency of the learned compensation model with aeromagnetic principles [27]; and (3) combining CEEMDAN and PGNN can improve compensation performance by leveraging the strengths of both data-driven and model-driven approaches, particularly under conditions of limited data quantity or quality. The key contributions of this work are as follows: (1) a hybrid compensation framework that integrates CEEMDAN-based feature decomposition with PGNN, thereby effectively addressing both linear and nonlinear aeromagnetic interference; (2) a novel loss function incorporating the T-L model, which enhances the interpretability and stability of the neural network while maintaining the flexibility of data-driven learning; and (3)

experimental vali- dation through simulation and real-world UAV flight tests, demonstrating that our method outperforms traditional model-driven (LS, ridge regression) and data-driven (BPNN,LSTM) approaches, particularly in challenging data conditions. This paper is structured as follows: Section 2 introduces the T-L model and the proposed CEEMDAN-PGNN method in detail, as well as the entire experimental process, including experimental equipment, data acquisition, and compensation effect evaluation indicators. Section 3 introduces the experimental results, compares different methods, and analyzes their performance. Section 4 conducts an in-depth analysis and discussion of the results, compares the similarities and differences with existing studies, and explores the significance and limitations of this work. Finally, Section 5 summarizes our research results as the conclusion of this paper.

2. Materials and Methods

2.1. T-L Model

A rectangular coordinate system was established to effectively describe the T-L model, as depicted in Figure 1. The measurement system was mounted on the aircraft body to measure the magnetic field, with the axes *x*, *y*, and *z* representing the three coordinate axes of the reference system. The origin *O* was located at the center of the drone. The vector magnetic field sensor's coordinate system aligned with the reference rectangular coordinate system that is shown in the figure. At a given moment, the measurement results were $T(t)$, $L(t)$, and $V(t)$, where **He** represents the real magnetic signal.

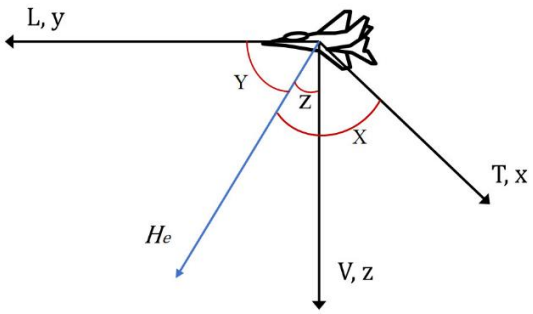

Figure 1. Reference coordinate system definition.

In aeromagnetic measurements, the value recorded by the airborne magnetometer represents the sum of the real magnetic field and the interference field generated by the aircraft [28]. This relationship can be expressed as a vector addition:

$$\mathbf{H_t} = \mathbf{H_e} + \mathbf{H_d} \tag{1}$$

where $\mathbf{H_d}$ is the aircraft magnetic interference field vector. Given that $H_e \gg H_d$, the output of the optical pump magnetometer can be considered equivalent to the sum of the projections of both the geomagnetic field and the interference field in the direction of the geomagnetic field:

$$H_t = H_e + H_d \cdot \cos\varphi = H_e + H_i \tag{2}$$

where φ represents the angle between the geomagnetic field and the interference field, He denotes the magnitude of the geomagnetic field vector, H_d denotes the magnitude of the interference field vector, and Hi is the projection of the interference field onto the direction of the geomagnetic field.

Fluxgate magnetometers are typically employed to measure the angle between the platform and the geomagnetic field direction [29]. In the reference rectangular coordinate system *oxyz*, the direction cosines u_1, u_2, and u_3 of the geomagnetic field are expressed as follows:

$$u_1 = \cos X(t) = \frac{T(t)}{\sqrt{T(t)^2 + L(t)^2 + V(t)^2}} \tag{3}$$

$$u_2 = \cos Y(t) = \frac{L(t)}{\sqrt{T(t)^2 + L(t)^2 + V(t)^2}} \tag{4}$$

$$u_3 = \cos Z(t) = \frac{V(t)}{\sqrt{T(t)^2 + L(t)^2 + V(t)^2}} \tag{5}$$

The magnetic interference generated by the aircraft is primarily due to the presence of ferromagnetic materials, the motor, and the electronic control system. This interference can be categorized into three types based on its source: the constant magnetic field, induced magnetic field, and eddy current magnetic field [30]. The constant magnetic field, which arises from the residual magnetism of ferromagnetic materials within the aircraft, remains unaffected by changes in the aircraft's attitude. This field can be represented in the body coordinate system as follows:

$$\mathbf{H_{perm}} = a_1\mathbf{i} + a_2\mathbf{j} + a_3\mathbf{k} \tag{6}$$

where $\mathbf{H_{perm}}$ denotes the constant magnetic field vector, while **i, j**, and **k** represent the unit vectors along the coordinate axes of the body coordinate system. The coefficients $a_i (i = 1, 2, 3)$ correspond to the components of the constant magnetic field along these axes. By projecting the constant field onto the direction of the geomagnetic field, the scalar value of the constant field H_{perm} can be expressed as follows:

$$H_{perm} = a_1u_1 + a_2u_2 + a_3u_3 = \sum_{i=1}^{3} a_iu_i \tag{7}$$

The induced magnetic field arises from the magnetization of ferromagnetic materials within the aircraft due to the geomagnetic field. This field is directly proportional to the strength of the geomagnetic field and can be expressed as follows:

$$\begin{aligned} \mathbf{H_{ind}} \quad &= H_e[(b_{11}u_1 + b_{12}u_2 + b_{13}u_3)\mathbf{i} \\ &+(b_{21}u_1 + b_{22}u_2 + b_{23}u_3)\mathbf{j} \\ &+(b_{31}u_1 + b_{32}u_2 + b_{33}u_3)\mathbf{k}] \end{aligned} \tag{8}$$

where $\mathbf{H_{ind}}$ denotes the induced magnetic field vector, and b_{ij} $(i, j = 1, 2, 3)$ represent the nine induced magnetic field coefficients. When projected in the direction of the geomagnetic field, the scalar value of the induced magnetic field H_{ind} can be expressed as follows:

$$\begin{aligned} H_{ind} &= H_e \begin{pmatrix} u_1 & u_2 & u_3 \end{pmatrix} \begin{pmatrix} b_{11} & b_{12} & b_{13} \\ b_{21} & b_{22} & b_{23} \\ b_{31} & b_{32} & b_{33} \end{pmatrix} \begin{pmatrix} u_1 \\ u_2 \\ u_3 \end{pmatrix} \\ &= H_e \sum_{i=1}^{3}\sum_{j=1}^{3} b_{ij}u_iu_j \end{aligned} \tag{9}$$

The eddy current magnetic field is generated when high conductivity materials within the aircraft intersect with the magnetic flux lines as the flight attitude changes. The components of this field along each axis are proportional to the rate of change in the geomagnetic field strength, as expressed by the following equation:

$$\begin{aligned} \mathbf{H_{eddy}} \quad &= H_e[(p_{11}u_1' + p_{12}u_2' + p_{13}u_3')\mathbf{i} \\ &+(p_{21}u_1' + p_{22}u_2' + p_{23}u_3')\mathbf{j} \\ &+(p_{31}u_1' + p_{32}u_2' + p_{33}u_3')\mathbf{k}] \end{aligned} \tag{10}$$

where $\mathbf{H_{eddy}}$ represents the eddy current magnetic field vector, with p_{ij} $(i, j = 1, 2, 3)$ denoting the nine eddy current magnetic field coefficients, and u_i' $(i = 1, 2, 3)$ representing the time derivative of u_i. The projection of the eddy current magnetic field in the direction of the geomagnetic field H_{eddy} can be expressed as follows:

$$\begin{aligned} H_{eddy} &= H_e(u_1 \quad u_2 \quad u_3)\begin{pmatrix} p_{11} & p_{12} & p_{13} \\ p_{21} & p_{22} & p_{23} \\ p_{31} & p_{32} & p_{33} \end{pmatrix}\begin{pmatrix} u_1' \\ u_2' \\ u_3' \end{pmatrix} \\ &= H_e \sum_{i=1}^{3}\sum_{j=1}^{3} p_{ij} u_i u_j' \end{aligned} \tag{11}$$

According to Equations (7), (9), and (11), the scalar value of magnetic interference can be expressed as follows:

$$\begin{aligned} H_i &= H_{perm} + H_{ind} + H_{eddy} \\ &= \sum_{i=1}^{3} a_i u_i + H_e \sum_{i=1}^{3}\sum_{j=1}^{3} b_{ij} u_i u_j + H_e \sum_{i=1}^{3}\sum_{j=1}^{3} p_{ij} u_i u_j' \end{aligned} \tag{12}$$

The formula above represents a T-L model expression that contains 21 coefficients. However, due to the symmetry of the induced magnetic field coefficient matrix, this expression can be reduced to one containing only 18 coefficients [31]:

$$H_i = \sum_{i=1}^{18} c_i A_i \tag{13}$$

where c_i (i = 1, 2, ...18) represents the 18 coefficients to be calculated, while A_i (i = 1, 2, ...18) is the coefficient matrix composed of the real magnetic field modulus, direction cosines, and their derivatives. During flight, n data points are continuously sampled, leading to the following matrix form corresponding to Equation 13:

$$\mathbf{H_i} = \mathbf{Ac} \tag{14}$$

where **c** is a column vector consisting of 18 magnetic compensation coefficients, **A** is a coefficient matrix consisting of A_i at n moments, and $\mathbf{H_i}$ is the platform interference magnetic field extracted from the optical pump data, which are defined as follows:

$$\mathbf{A} = \begin{bmatrix} A_1(1) & A_2(1) & \cdots & A_{18}(1) \\ A_1(2) & A_2(2) & \cdots & A_{18}(2) \\ \vdots & \vdots & \ddots & \vdots \\ A_1(n) & A_2(n) & \cdots & A_{18}(n) \end{bmatrix}, \mathbf{H_i} = \begin{bmatrix} H_i(1) \\ H_i(2) \\ \vdots \\ H_i(n) \end{bmatrix}, \mathbf{c} = \begin{bmatrix} c_1 \\ c_2 \\ \vdots \\ c_{18} \end{bmatrix} \tag{15}$$

The compensation coefficient can be determined using least squares regression as follows:

$$\mathbf{c} = (\mathbf{A}^T\mathbf{A})^{-1}\mathbf{A}^T\mathbf{H_i} \tag{16}$$

To address the ill-posed problem arising from multicollinearity, the coefficient c can alternatively be calculated using the ridge regression method [10]:

$$\mathbf{c} = (\mathbf{A}^T\mathbf{A} + \lambda\mathbf{I})^{-1}\mathbf{A}^T\mathbf{H_i} \tag{17}$$

where λ is the regularization coefficient.

2.2. CEEMDAN Algorithm

In aeromagnetic compensation, the raw magnetic field signal is often nonlinear and nonstationary, making it challenging for traditional machine learning models to extract effective features. To address this, empirical mode decomposition (EMD) and its improved versions, ensemble empirical mode decomposition (EEMD) [34] and CEEMDAN, have been widely applied for signal preprocessing. EMD decomposes a signal into a set of intrinsic mode functions (IMFs) through an iterative process. However, it suffers from mode mixing, where

IMFs contain components of widely different scales, leading to poor decomposition quality. To mitigate this issue, EEMD was proposed, introducing white noise to force the decomposition into more distinct modes. While EEMD significantly reduces mode mixing, it has two main limitations: (1) residual noise contamination, where each IMF in EEMD contains residual noise due to the added white noise, thereby affecting the stability and accuracy of the decomposition; and (2) non-complete reconstruction, where the original signal cannot be perfectly reconstructed because EEMD does not fully compensate for the introduced noise. CEEMDAN was developed as an enhancement over EEMD to further improve decomposition accuracy and ensure complete signal reconstruction. The key advantages of CEEMDAN over EEMD are as follows: (1) Elimination of residual noise as CEEMDAN introduces a new noise-assisted decomposition strategy, where noise is adaptively added to each stage of the decomposition. This ensures that each IMF is extracted with minimal interference, leading to more stable and reliable decomposition results. (2) Complete signal reconstruction as, unlike EEMD, CEEMDAN ensures that the sum of all IMFs and the final residual perfectly reconstruct the original signal, preserving critical information for subsequent analysis. (3) Improved mode separation, which is achieved by refining the iterative noise-assisted decomposition process, where CEEMDAN generates IMFs with better mode separation, thus reducing the risk of mode aliasing and ensuring that each IMF represents a distinct frequency component. (4) Better adaptability to nonstationary signals, which is achieved given that aeromagnetic interference contains both stationary and nonstationary components, and CEEMDAN has the ability to handle complex signal variations, thereby enhancing its effectiveness in feature extraction. The flowchart of CEEMDAN is shown in Figure 2. The specific steps are as detailed below.

(1) Add white noise: White noise of different amplitudes is added to the original signal $s(t)$ to generate multiple noisy signals.

$$s_i(t) = s(t) + \epsilon_0\, n_i(t) \tag{18}$$

where ϵ_0 is the noise amplitude, $n_i(t)$ is the white noise sequence, and i is the number of different noise realizations.

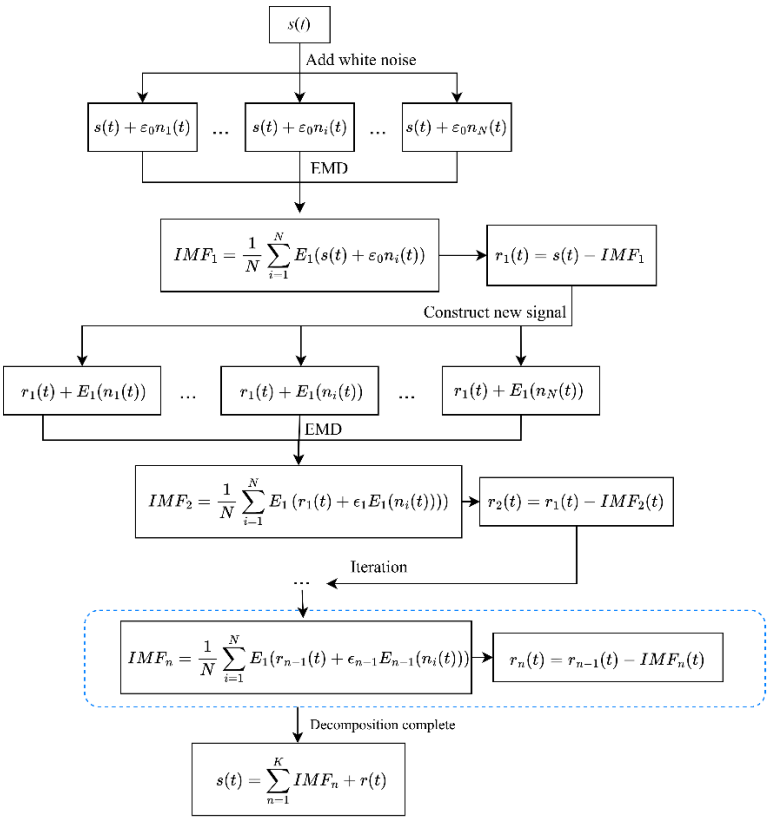

Figure 2. A flowchart of the CEEMDAN algorithm.

(2) Perform EMD decomposition: EMD decomposition is performed on each noisy signal $s_i(t)$ to obtain its first IMFs. Then, the average of the first IMFs of all noisy signals is calculated to obtain the first complementary IMFs:

$$IMF_1 = \frac{1}{N}\sum_{i=1}^{N} E_1(s(t) + \epsilon_0\, n_i(t)) \tag{19}$$

where E_n (*) is defined as the nth mode component of the EMD.

(3) Calculate the first residual: The first complementary IMFs from the original signal $s(t)$ are subtracted to obtain the first residual signal:

$$r_1(t) = s(t) - IMF_1 \tag{20}$$

(4) Constructing a new signal is achieved with the following:

$$s_1(t) = r_1(t) + E_1(n_i(t)) \tag{21}$$

EMD decomposition is performed on the constructed new signal. Then, the second modal component is obtained:

$$IMF_2 = \frac{1}{N}\sum_{i=1}^{N} E_1(r_1(t) + \epsilon_1\, E_1(n_i(t))) \tag{22}$$

(5) Iterative processing: Steps 3 and 4 are repeated to obtain the nth residual signal and the n + 1th IMFs:

$$r_n(t) = r_{n-1}(t) - IMF_n(t) \tag{23}$$

$$IMF_{n+1} = \frac{1}{N}\sum_{i=1}^{N} E_1(r_n(t) + \epsilon_n\, E_n(n_i(t))) \tag{24}$$

(6) Stopping criteria: The iteration process terminates when the residual signal $r_n(t)$ becomes a monotonic function or when its energy is negligible. At this point, the original signal can be expressed as follows:
where K is the number of IMFs of CEEMDAN, and $r(t)$ is the final residual.

$$s(t) = \sum_{n=1}^{K} IMF_n + r(t) \tag{25}$$

2.3. Physics-Guided Neural Network

2.3.1. Basic Structure

Conventional neural network aeromagnetic compensation methods completely rely on data-driven methods to eliminate magnetic interference. These methods as black-box models, which are inherently difficult to interpret and involve complex input features. The variability in input features can result insignificantly inconsistent compensation outcomes. To overcome these limitations, we propose a novel compensation method that integrates both physical model-driven and data-driven frameworks. This method utilizes sequences decomposed by CEEMDAN as feature inputs for the network model, eliminating the need for extensive experimentation to identify optimal input features. The decomposed signals exhibit more distinct characteristics, allowing the neural network to extract the necessary information more effectively and efficiently. The proposed method is illustrated in Figure 3. A neural network based on a common data-driven framework [32] is illustrated in Figure 4. The network takes, as input, the time coordinates of the magnetic signal, the three-component fluxgate data, the aircraft's direction cosines, and other relevant variables, with the real magnetic signal as the output. In contrast, our proposed method employs the total magnetic field signal sequence, which is decomposed by CEEMDAN, as the network input, with the interference field as the output. The final clean magnetic field is obtained by subtracting the predicted interference field Hi from the input total magnetic field Ht. This method integrates a physical model with the data-driven framework by embedding the T-L model into the final output, where the magnetic interference coefficient c serves as a trainable parameter that is synchronously updated with the network weights and biases.

2.3.2. T-L Model Embedded Loss Function

Inspired by the concept of PGNN [23], this paper integrated the T-L model with a neural network model. This combined method guides the neural network in learning a physically consistent solution. The first part of the loss function is defined by the T-L model:

$$Loss_1(\mathbf{c}; H_i) = \frac{1}{N}\|\mathbf{Ac} - H_{ilabel}\|_2^2 \tag{26}$$

The loss function of the T-L model constraint is a function of the neural network input and output, where **c** is the compensation coefficient, H_i is the model prediction value, H_{ilabel} is the true value, and N is the data length. The vector **A** is calculated from the model input H_t, output H_i, and the direction cosines u_i and their derivatives.

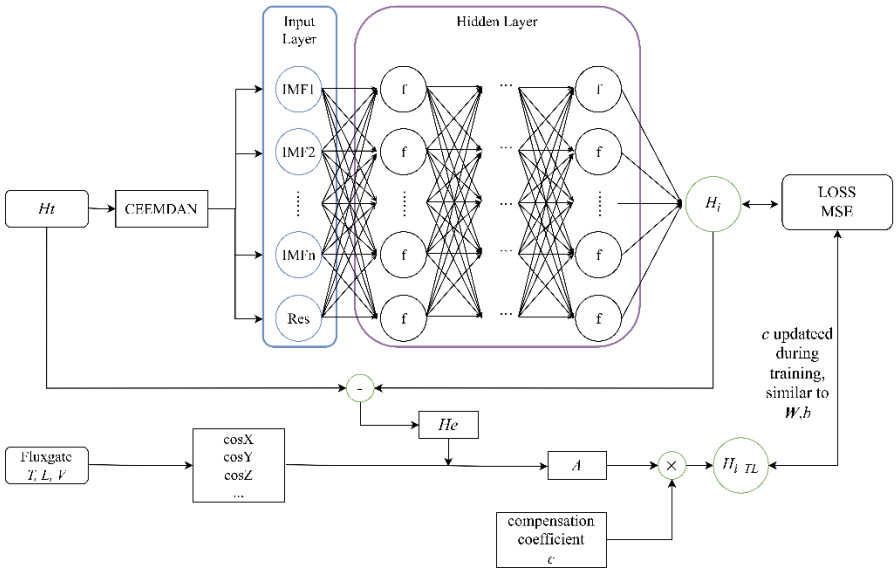

Figure 3. A network structure based on complete ensemble empirical mode decomposition with adaptive noise and physics-guided neural network (CEEMDAN-PGNN): the input data are the total magnetic field with interference, and the output is the interference.

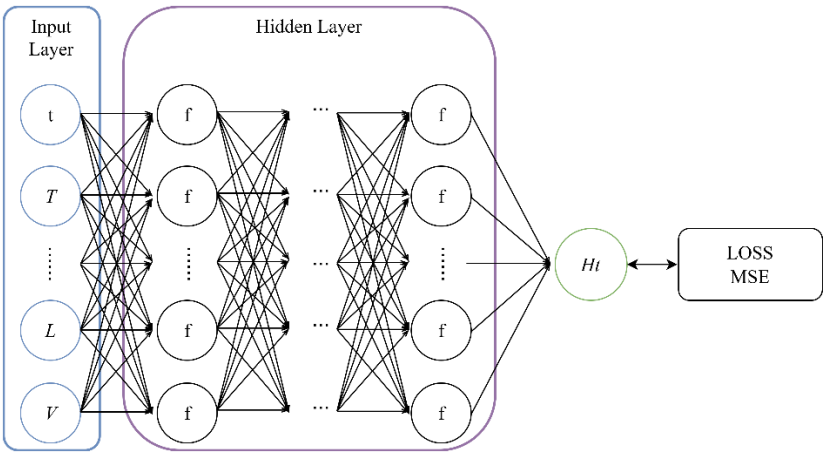

Figure 4. A network structure based on BP neural network (BPNN): the input is the measured data and the output is the clean magnetic field.

The specific calculation method is shown in Equations (3)-(5) and (12)-(14), and it will not be repeated here. This method combines the output of the neural network with the input information in the loss function, and it guides the output of the PGNN to converge to the direction defined by Equation (13).

The second part of the loss function is constrained by the data:

$$Loss_2(\boldsymbol{\theta}; H_i) = \frac{1}{N}\|H_i - H_{ilabel}\|_2^2 \tag{27}$$

where $\boldsymbol{\theta}$ represents the weights and bias of the neural network.

In addition, L2 regularization terms were introduced to penalize model parameters [33], mitigate overfitting, and enhance the robustness of the neural network model. The final loss function is expressed as follows:

$$Loss(\boldsymbol{\theta}, \mathbf{c}; H_i) = \alpha \, \mathrm{Loss}_1(\mathbf{c}; H_i) + Loss_2(\boldsymbol{\theta}; H_i) + \beta \|\boldsymbol{\theta}\|_2^2 \tag{28}$$

where the hyperparameters α and β represent the strength of the physical model and regularization constraints. When α is 0, the loss function only becomes constrained by the data.

In the network model, the structure is organized into an input layer, hidden layers, and an output layer. The network's input feature is denoted by h, and the connections between the neural network nodes are represented by the parameters $(\boldsymbol{\omega}, \boldsymbol{b}) = (\omega^1, b^1, \omega^2, b^2, \ldots, \omega^l, b^l)$, where ω^l is the weight connecting the (l-1)th layer to the lth layer and b^l is the bias of the lth layer. During forward propagation, the input and output of a neural network node are as follows:

$$h_{p,in}^{(l+1)} = \sum_{i=1}^{N_l} h_{i,out}^{(l)} \omega_i^{(l+1)} + b^{(l+1)} \tag{29}$$

$$h_{p,out}^{(l+1)} = f\left(h_{p,in}^{(l+1)}\right) \tag{20}$$

where N_l is the number of nodes in layer l, $f(\cdot)$ is the activation function, and the superscripts l and $l + 1$ indicate the number of layers.

During back propagation, the gradients of the network parameters are updated using the chain rule.

$$\frac{\partial Loss(\boldsymbol{\theta}, \boldsymbol{c})}{\partial \theta_{ij}^{(l)}} = \frac{\partial Loss(\boldsymbol{\theta}, \boldsymbol{c})}{\partial h_{i,m}^{(l)}} \frac{\partial h_{i,m}^{(l)}}{\partial \theta_{ij}^{(l)}} = \delta_i^{(l)} h_{j,out}^{(l-1)} \tag{31}$$

where the first subscript i represents the i-th node in the l-th layer, and the second subscript j represents the j-th node in the (l-1)th layer. In addition, δ is the error term, which is defined as follows:

$$\delta_i^{(l)} = \sum_{j=1}^{N_{l+1}} \delta_j^{(l+1)} \frac{\partial h_{j,in}^{(l+1)}}{\partial h_{i,out}^{(l)}} \frac{\partial h_{i,out}^{(l)}}{\partial h_{i,in}^{(l)}} \tag{32}$$

$$\delta^{(L)} = \frac{\partial Loss(\boldsymbol{\theta}, \boldsymbol{c})}{\partial h_{out}^{(L)}} \frac{\partial h_{out}^{(L)}}{\partial h_{in}^{(L)}} \tag{33}$$

The input features undergo forward propagation to generate the output. Subsequently, the gradients of each weight and bias in the neural network are computed through back propagation. During training, these parameters are updated using the gradient descent algorithm to minimize the loss function. The compensation coefficient **c** is initialized by (17) and is also updated using gradient descent during network training.

2.4. Experimental Setup

2.4.1. Compensation Process

The specific steps of the proposed method are as detailed below.

(1) Flight Experiments:

Flight experiments and simulations are conducted to obtain the datasets, with the detailed methodology described in the subsequent section. Notably, compared to conventional neural networks, the proposed CEEMDAN and physical model-guided neural network requires fewer datasets to achieve superior compensation performance.

(2) Dataset Generation:

The collected data are eigendecomposed, and the generated sequences and the actual interference field H_{ilabel} obtained by bandpass filtering are assembled into a dataset.

(3) Compensation Coefficient Initialization:

The compensation coefficient **c** is treated as a set of trainable parameters within the network. Its initial value is computed based on the T-L model.

(4) Model Training:

The model is trained using the dataset from Step 2, employing the ReLU activation function, Adam optimization algorithm, and MSE loss function.

(5) Hyperparameter Optimization:

The hyperparameters to be optimized include the network architecture, loss function weights, batch size, etc. The training results under various parameter combinations are assessed to determine the optimal hyperparameters.

(6) Compensation Test:

The trained network is tested to evaluate its compensation effectiveness and robust- ness, and the overall model performance is assessed.

The detailed network parameter settings are shown in Table 1.

Table 1. Parameter settings for the network.

Parameters	**Configuration**
Input layer	The sequences of the total magnetic field signal after decomposition by CEEMDAN
Output layer	Magnetic interference
Hidden layer structure	10-10-16
Batch size	512
Epoch size	500
Optimizer	Adam
Loss criterion	MSE loss

2.4.2. Flight Experiment

To validate the effectiveness of the proposed method, a multi-rotor UAV was employed to conduct flight tests for collecting aeromagnetic data. The complete test system is illustrated in Figure 5. The UAV platform utilizes GPS for positioning. A cesium optical pump magnetometer and a fluxgate magnetometer are rigidly attached to the data acquisition system via carbon rods. The optical pump magnetometer model is CAS-18-VL, which is used to measure the scalar magnetic field in space. The fluxgate magnetometer model is Mag-03MS1000, which is produced by Bartington, UK, and it is mainly used to obtain the attitude information of the UAV. The specific parameters are shown in Table 2.

Table 2. The technical specifications of the magnetic sensors.

Technical indicators	**Mag-03MS1000**	**CAS-18-VL**
Measuring range	±70/100/250/500/1000μT	10000-105000nT
Noise level	6~10pT/sqrt Hz@1Hz	0.3pT/sqrt Hz@1Hz
Size	32×32×152mm	Φ53×130mm
Weight	0.16kg	0.5kg

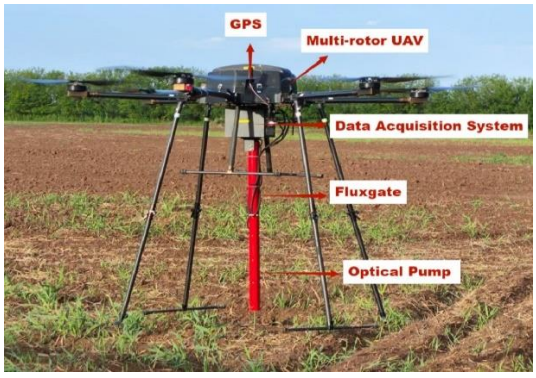

Figure 5. The unmanned aerial vehicle (UAV) experimental platform.

Since aeromagnetic interference originates from platform-induced disturbances, specific flight maneuvers are necessary to effectively excite and separate different interference components. Inspired by the Leliak flight pattern [8], we designed a controlled flight maneuvering strategy tailored for UAVs to evaluate the compensation performance under different attitude variations. (1) Pitch oscillation maneuvers were performed by tilting the UAV forward and backward within a ±5° range while maintaining a fixed heading. This motion primarily affects the induced magnetic field, which arises from the magnetization of the UAV's ferromagnetic components in response to the geomagnetic field. The induced field varies with changes in UAV orientation, making pitch oscillation essential for characterizing and compensating for these variations. (2) Yaw oscillation maneuvers were conducted by rotating the UAV left and right around its vertical axis with a yaw range of ±10°. This maneuver primarily impacts the eddy current magnetic field, which is generated when conductive materials within the UAV interact with the geomagnetic field as the aircraft undergoes angular motion. Since eddy current effects are highly dependent on the rate of change of the UAV's heading, these oscillations allow us to assess how well the compensation method adapts to such dynamic interference. (3) Roll oscillation maneuvers were executed by tilting the UAV sideways within ±5° range along its longitudinal axis. Unlike pitch and yaw, which predominantly influence the induced and eddy current fields, roll oscillations introduce a combination of constant and induced field variations. This is be- cause the residual magnetization of UAV components interacts with the changing attitude, leading to complex magnetic disturbances that require compensation. (4) In addition to these controlled maneuvers, a level flight at a constant speed was performed as a baseline measurement. This condition provided an essential reference for assessing the overall interference levels and evaluating the compensation effectiveness under steady-state flight conditions. Each maneuver was performed along a rectangular flight path, covering the four cardinal directions (north, east, south, and west), as depicted in Figure 6. These maneuvers ensure that the dataset contains diverse motion-induced magnetic disturbances, which are necessary for evaluating the robustness of the proposed compensation method.

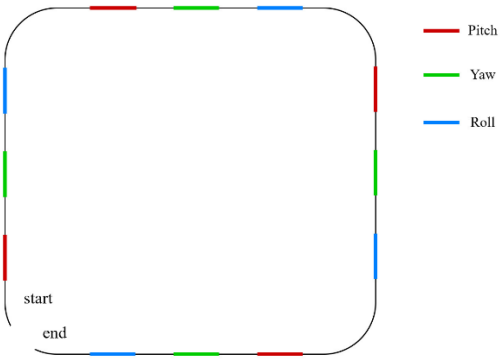

Figure 6. The UAV flight trajectory and maneuvers performed to obtain experimental data.

2.5. Evaluation Indicators

The most commonly used compensation performance evaluation indicators in the field of aeromagnetic compensation are standard deviation (STD) and improvement ratio (IR) [35,36], which are defined as follows:

$$STD = \sqrt{\frac{1}{n}\sum_{i=1}^{n}(x_i - \overline{x})^2} \tag{34}$$

$$IR = \frac{STD_u}{STD_c} \tag{35}$$

In the formula, STD_u represents the standard deviation of magnetic interference before compensation, while STD_C denotes the standard deviation of residual magnetic interference after compensation, where $\overline{x}$ represents the arithmetic mean of the interference field, x_i represents the magnetic field interference value at the sampling point,

and n refers to the number of sampling points. A higher improvement ratio corresponds to a more effective compensation.

3. Results

3.1. Ablation experiments

This experiment aimed to verify the effectiveness of the T-L model's embedding loss function, which is represented by Equation (28). We adjusted the weight α of the physical model loss function, compared the compensation performance under different circum- stances, and determined the most suitable hyperparameter α. When α = 0, the physical model no longer constrained the loss function. As illustrated in Figure 7, incorporating the physical model constraint into the loss function enhanced the compensation performance. When the α value was either too small or too large, the loss function was predominantly influenced by the data or the physical model, leading to a larger standard deviation (STD) of the compensated data and a lower improvement ratio (IR). Through empirical analysis, we selected α = 1.2, as it provides an optimal balance between physical constraint effects and the network's ability to learn from data. Similarly, the hyperparameter β was chosen as 0.1 to ensure stable and effective compensation performance.

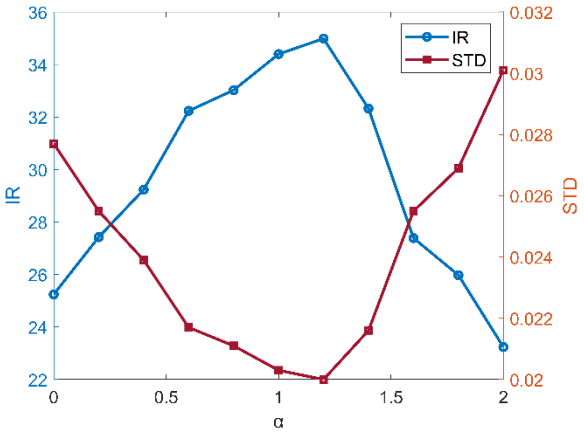

Figure 7. The influence of the physical model constraint weight α on the compensation effect. The optimal weight was found to be 1.2.

3.2. Simulation Experiments

To demonstrate the superiority of our method, we conducted comparative experiments to compensate the simulated aeromagnetic data using three techniques: the proposed method, model-driven methods, and data-driven methods. The model-driven methods included LS and Ridge regression, while the data-driven methods consisted of BPNN and LSTM. In the data-driven methods, the input features included time t, direction cosines of the magnetic vector ui, and the measured magnetic field signals Ht. The magnetic interference, generated by the UAV during flight, was simulated using the Leliak flight method described in Section2.4.2. In this simulation, the geomagnetic field intensity was set to 50,000 nT, with a magnetic inclination of 50° and a magnetic declination of -5°. Figures 8 and 9present the three components of the aeromagnetic data and the interference field obtained through simulation during the flight.

The compensation results of the simulated data are shown in Figure 10 and Table 3. Figure 10 shows the effects of five different methods before and after the simulated maneuvering interference compensation. CEEMDAN decomposition, as an adaptive form of principal component analysis, effectively extracts more regular signal features, making it easier for the subsequent neural network to learn. Experimental results show that our proposed method achieved the best compensation performance. The results were as follows: The original interference had a standard deviation of 0.6998. The LS method reduced the standard deviation to 0.08, resulting in an IR of 8.7469. The Ridge regression method reduced the standard deviation to 0.077, with an IR of 9.0877. The BPNN reduced the standard deviation to 0.026, achieving an IR of 26.9136. The LSTM reduces the standard deviation to 0.022, yielding an IR of 31.807. The proposed CEEMDAN-PGNN method reduced the standard deviation to 0.02, with an IR of 34.9877.

These results demonstrate that the proposed method not only significantly reduces the magnetic interference, but also outperforms both traditional model-driven and modern data-driven approaches, especially in terms of achieving the highest improvement ratio and lowest residual interference.

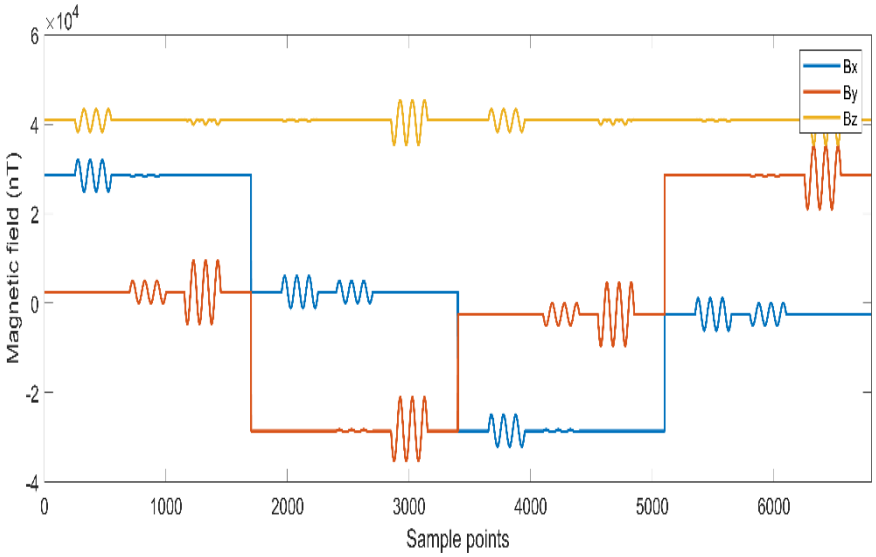

Figure 8. Simulation data of three components of the total magnetic field, as simulated by MATLAB, which were used as input for the least squares (LS),ridge regression (RR), BPNN, and long short-term memory neural network (LSTM) methods.

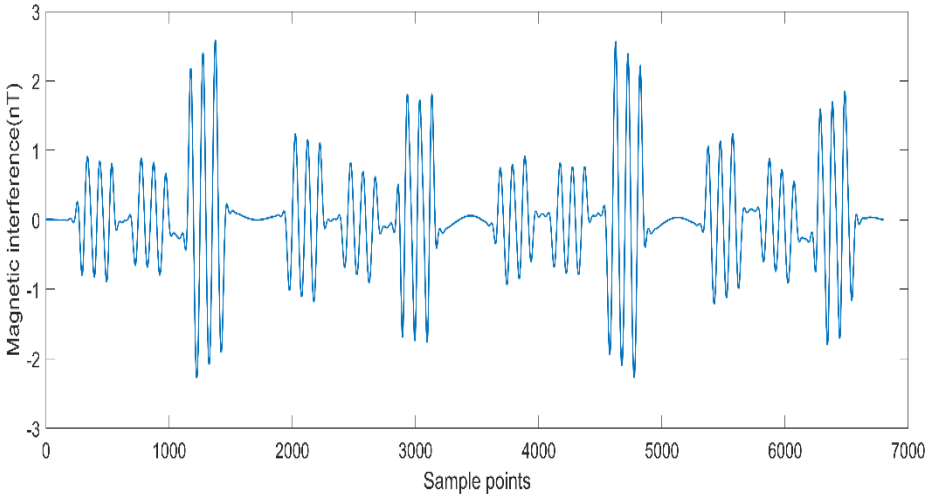

Figure 9. Magnetic interference of the flight simulation (what needed compensation).

Table 3. Detailed compensation results of the simulation data (the smaller the standard deviation (STD), the higher the improvement ratio (IR), and the better the compensation effect).

Method	**STD**	**IR**
Raw	0.6998	1
LS	0.0800	8.7469
Ridge	0.0770	9.0877
BPNN	0.0260	26.9136
LSTM	0.0220	31.8070
CEEMDAN-PGNN	**0.0200**	**34.9877**

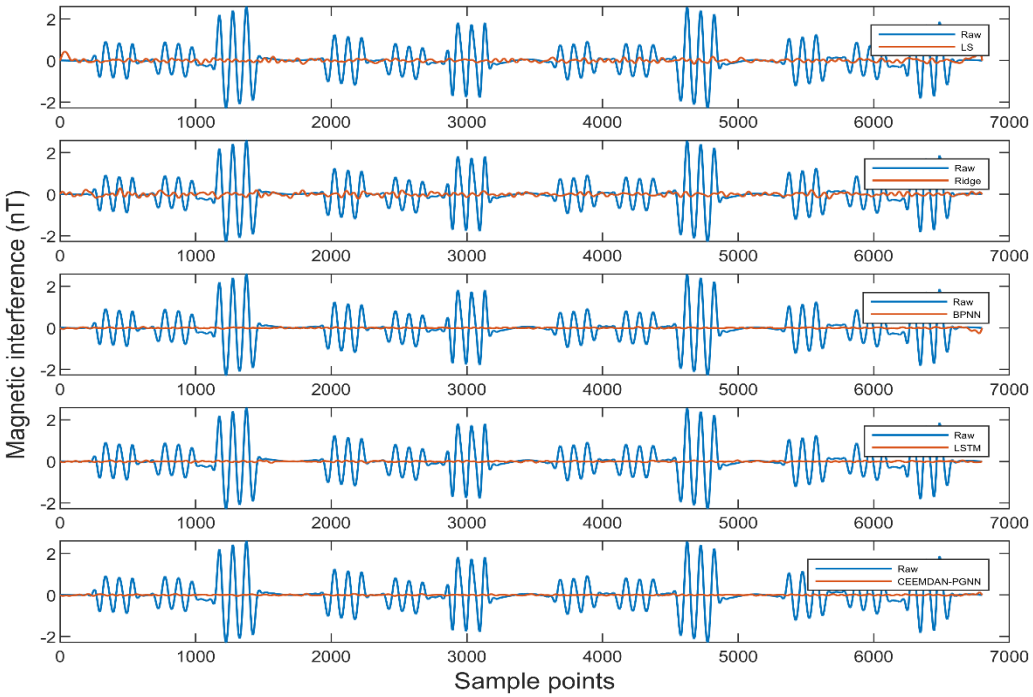

Figure 10. Compensation results of the simulation data. The residual disturbance in the magnetic field data before and after compensation is shown. Raw represents the original magnetic interference, LS represents the least squares algorithm, Ridge represents the ridge regression algorithm, BPNN represents the BP neural network, LSTM represents the long short-term memory neural network, and CEEMDAN-PGNN is the proposed method.

3.3. Robustness Analysis about the Data Quality

To evaluate the robustness of our proposed method under low data quality conditions, we introduced varying degrees of Gaussian noise and colored noise into the simulated aeromagnetic data. Gaussian noise was added to the data to simulate the random fluctuations that typically occur in real-world measurements (while colored noise mimics more structured disturbances that can arise from electronic equipment or environmental factors). We tested the method by introducing noise levels ranging from low to high, adjusting the noise standard deviation to simulate different levels of data corruption. Figures 11and 12 shows the three-component data of the magnetic field with a signal-to-noise ratio of 15 dB and the corresponding interference field

The compensation results under these noisy conditions are presented in Figures 13 and Table 4. The LS and ridge regression methods only achieved an IR of 5.8347 and 5.7156, while the BPNN and LSTM methods achieved an IR of 20.0045 and 23.3386. The CEEMDAN-PGNN method achieved the highest IR of 27.4572. Model-driven methods, particularly LS and ridge regression, were found to be highly susceptible to nonlinear noise. This is because these methods are fundamentally based on linear assumptions, which do not adequately account for the nonlinear disturbances introduced by noisy data. As a result, their compensation performance significantly degraded in the presence of both Gaussian and colored noise. Specifically, these methods struggle to effectively model the complex relationships between the magnetic interference and noisy data, leading to large residual errors. In contrast, data-driven methods like BPNN and LSTM perform better under noisy conditions, especially with nonlinear noise. These methods are more flexible due to their ability to learn complex, nonlinear mappings from data. However, even data-driven models show a noticeable decline in performance as the noise level increases, particularly when the data quality becomes poor. The performance degradation is reflected in a higher standard deviation of the residual magnetic interference and a lower improvement ratio.

Our proposed method, CEEMDAN-PGNN, combines the strengths of both model-driven and data-driven approaches, leading to superior performance in noisy environments. By first applying CEEMDAN to decompose the noisy signal into more distinct components, the network is better able to focus on the relevant features of the data while reducing the impact of noise. The PGNN further enhances the model's ability to maintain stable compensation by incorporating physical constraints that guide the learning process, even in the presence of substantial noise. This hybrid approach reduces the sensitivity of the model to nonlinear interference and ensures consistent and accurate compensation performance across varying levels of data corruption.

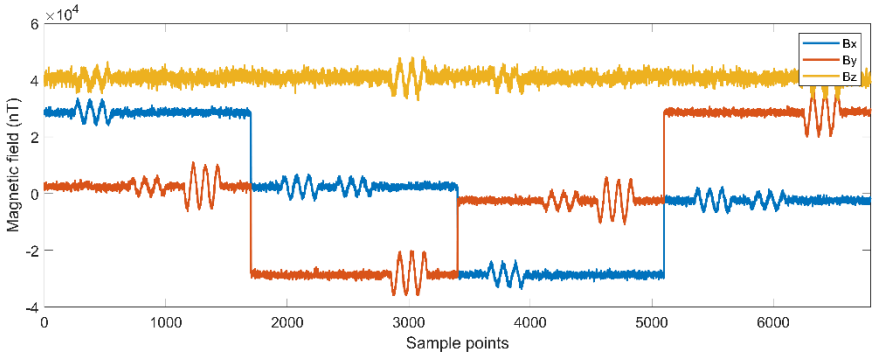

Figure 11. The simulated data of the three components of a total magnetic field with noise.

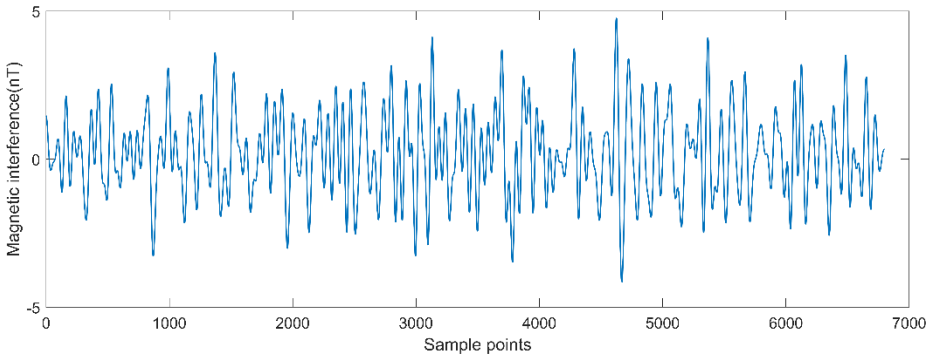

Figure 12. Simulated magnetic interference with noise.

Table 4. Detailed compensation results of the added noise data.

Method	STD	IR
Raw	1.4003	1
LS	0.2400	5.8347
Ridge	0.2450	5.7156
BPNN	0.0700	20.0045
LSTM	0.0600	23.3386
CEEMDAN-PGNN	**0.0510**	**27.4572**

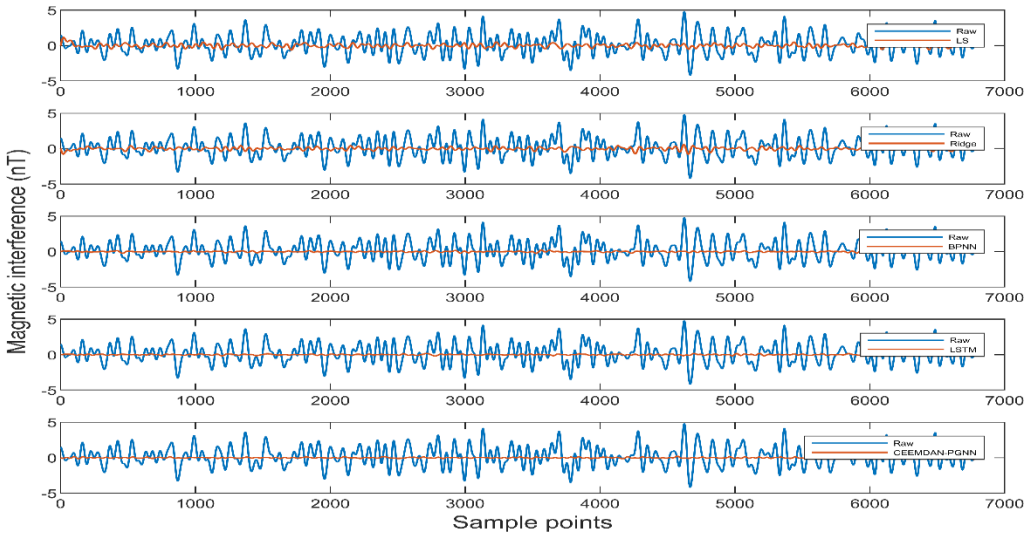

Figure 13. Compensation results of added noise data (from top to bottom, comparisons of the residual interference and the original interference of the magnetic field data after compensation by the LS, Ridge, BPNN, LSTM and CEEMDAN-PGNN methods).

3.4. Robustness Analysis about the Data Quantity

To demonstrate the effectiveness of our method under limited data, we trained the network using different amounts of simulation data. Figure 14 shows the compensation performance on a consistent test set. The vertical axis represents the standard deviation of the residuals after compensation, while the horizontal axis corresponds to the number of flights used to train the network. The number of flights was directly related to the size of the dataset, with fewer flights corresponding to smaller datasets.

As expected, data-driven neural network methods (such as BPNN and LSTM) exhibit a clear dependency on the size of the dataset. With a smaller dataset, the performance of these methods deteriorates significantly as the network has fewer data to learn the com- plex relationships between the magnetic interference and the observed data. This results in higher residuals (larger STD) and lower compensation effectiveness. In contrast, our proposed method, CEEMDAN-PGNN, demonstrated strong compensation performance and stability even when the training dataset was limited. Even with smaller datasets, the CEEMDAN step effectively decomposes the noisy magnetic signals into distinct components, enabling the PGNN to learn the most relevant features of the data. By combining physical constraints with data-driven learning, our method is less reliant on the volume of data and can still achieve high-quality compensation, maintaining low residuals and stable performance across different dataset sizes.

This result highlights the robustness of the proposed method in scenarios with limited data, which is where traditional data-driven methods often fail. The ability of CEEMDAN-PGNN to maintain consistent compensation performance with smaller datasets makes it particularly suitable for real-world applications, where data acquisition maybe costly or time consuming.

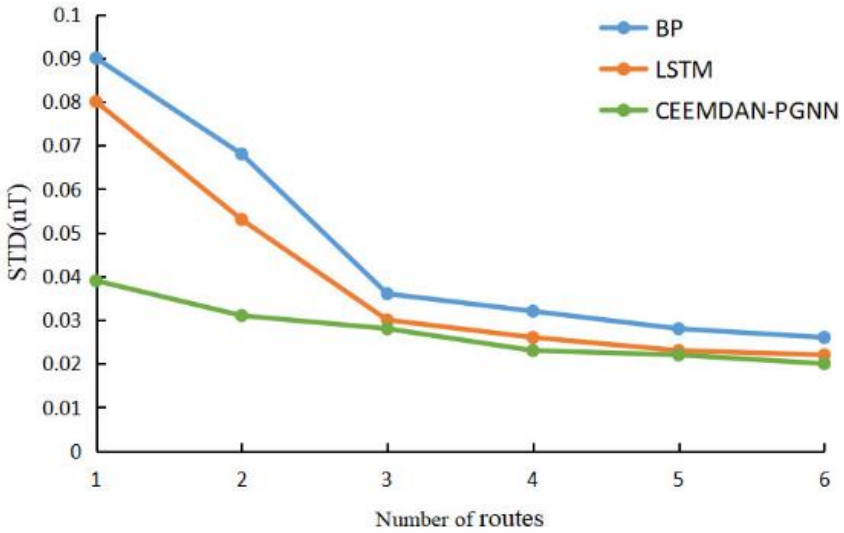

Figure 14. The compensation effect under different data quantities (the horizontal axis represents the amount of training set data, and the vertical axis represents the compensation results on the unified test set).

3.5. Real Flight Test

To validate the effectiveness of the proposed method under real-world conditions, we conducted flight tests using the method and equipment described in Section 2.4.2. Figure 15 shows the original total magnetic field data *Ht* and its decomposed sequences. The original data collected during the flight was significantly affected by magnetic interference, making compensation essential for accurate interpretation. To further illustrate the performance, we have reported the IR and the STD of the residual magnetic field after compensation. Our method achieved the highest improvement ratio, significantly reducing the residual interference when compared to traditional methods. The compensation results are presented in Figure 16 and Table 5. In the actual flight data, the proposed method achieved significant improvements, reducing the magnetic interference amplitude in the original data from 6 nT to 0.1 nT. This result demonstrates the effectiveness of the proposed method in real- world conditions and highlights its strong potential for practical application. These results confirm that the CEEMDAN-PGNN method not only provides precise compensation for simulated data, but it also performs robustly in real-world flight tests, where data quality and interference are often more complex.

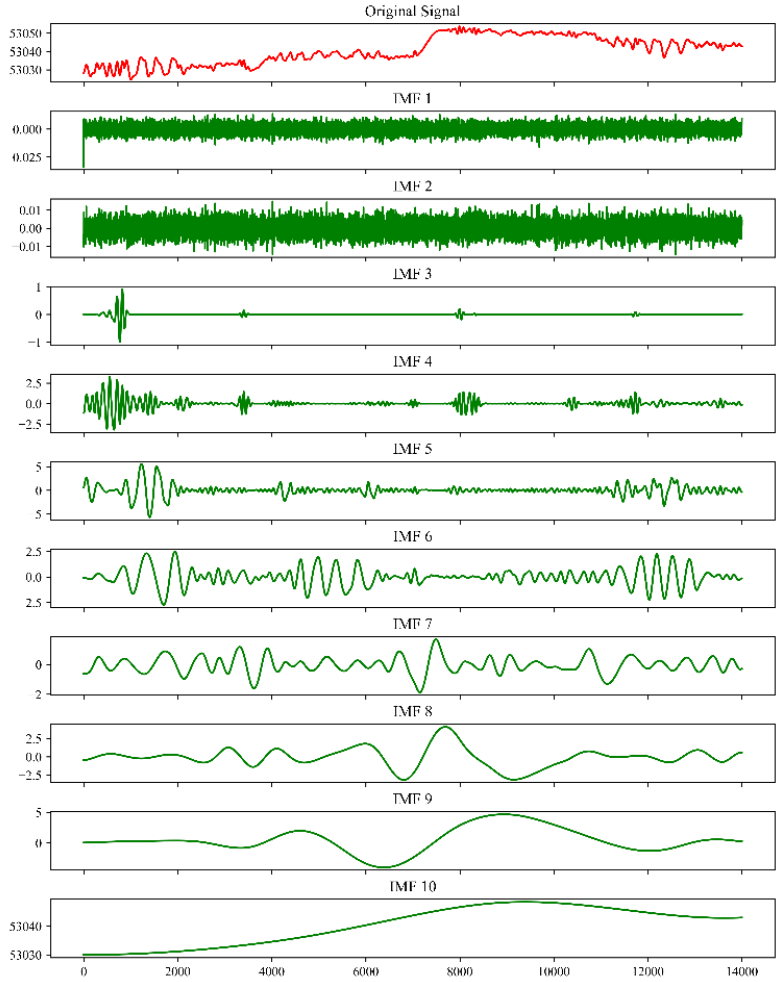

Figure 15. The decomposition results of the original signal Ht by CEEMDAN, where Ht is the actual measured data with interference.

Table 5. Detailed compensation results of real flight data.

Method	**STD**	**IR**
Raw	1.7512	1
LS	0.3438	5.0940
Ridge	0.3452	5.0733
BPNN	0.1794	9.7631
LSTM	0.1384	12.6556
CEEMDAN-PGNN	**0.1000**	**17.5119**

Results from both the simulated and real flight data experiments show that the pro- posed CEEMDAN-PGNN approach outperformed both model-driven and data-driven approaches. The main reasons for this are the following: (1) Effective signal decomposition was achieved using CEEMDAN as it is particularly good at handling complex nonlinear disturbances that often occur in aeromagnetic measurements. Traditional model-driven approaches such as LS and ridge regression rely on linear models that have difficulty.

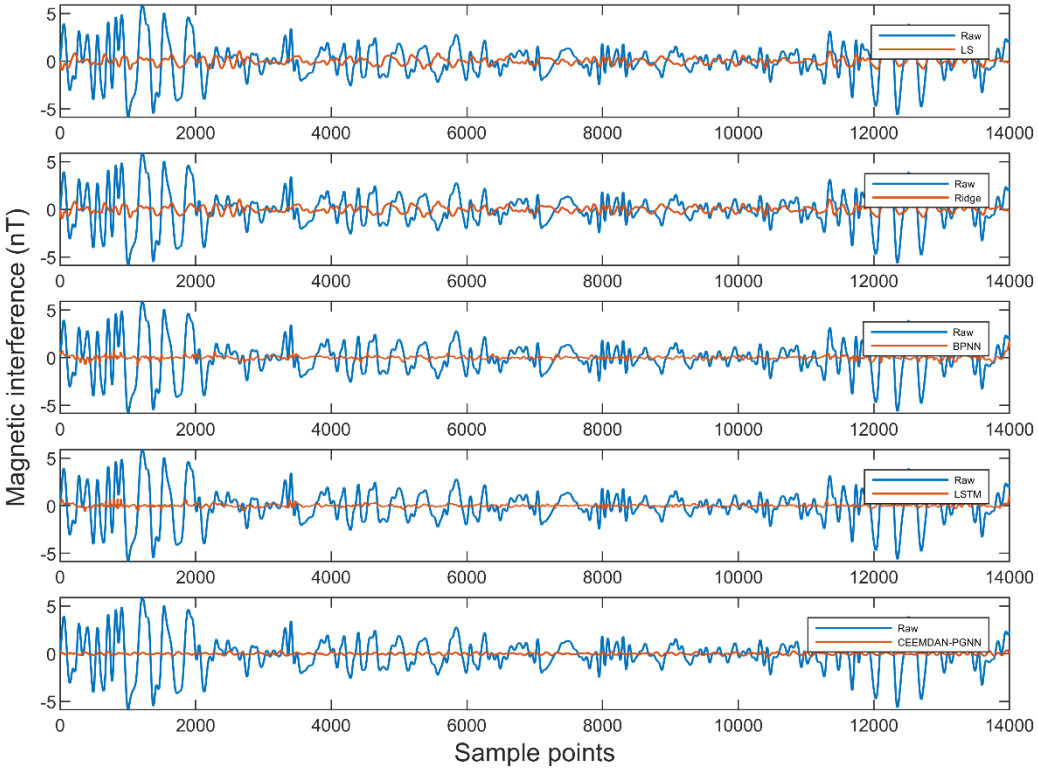

Figure 16. Real flight data compensation results (from top to bottom, the comparison between the residual interference and the original interference of the magnetic field data after compensation by the LS, Ridge, BPNN, LSTM and CEEMDAN-PGNN methods).

accounting for the nonlinear nature of disturbances, especially when flight conditions are variable. On the other hand, CEEMDAN decomposes the signal into different intrinsic mode functions, which allows for a more accurate decomposition of disturbance components, making it easier for the neural network to learn and compensate for these disturbances. (2) PGNN helped to alleviate the overfitting problem that is common in purely data-driven approaches by integrating the physical model of aeromagnetic disturbances into the neural network. Unlike BPNN and LSTM, which rely entirely on large datasets for learning, PGNN benefits from physical constraints that guide the network to find solutions consistent with the underlying physical processes. This is particularly advantageous when the dataset is limited or noisy, as demonstrated by the robustness of our approach under conditions of low data quality and quantity. (3) Both model and data-driven methods tended to lose accuracy as the noise increased, but CEEMDAN-PGNN remained stable due to its combination of the decomposition method and physical constraints, which helps filter out noise and focus on the real signal.

4. Discussion

The proposed method advances the state of the art in aeromagnetic compensation by combining data-driven learning with physical modeling. Existing methods, such as the Tolles–Lawson model and various regression-based techniques, focus primarily on linear assumptions and often require well-controlled flight paths to be effective. However, these methods have limited applicability when dealing with nonlinear disturbances or when there is insufficient high-quality data. Recent approaches, including those based on BPNN and LSTM, show improvements in handling nonlinear data, but they still face challenges in generalization when data are noisy or scarce. Our method, by leveraging CEEMDAN's feature decomposition and PGNN's physical guidance, represents a significant improvement over purely data-driven or purely model-driven approaches. It bridges the gap between traditional methods and modern machine learning techniques, providing a more flexible, robust, and interpretable solution to aeromagnetic compensation. While the CEEMDAN-PGNN method shows clear advantages, it is not without limitations: (1) CEEMDAN demonstrates computational complexity as the use of CEEMDAN for signal decomposition adds computational overhead, especially when processing large datasets. (2) There is a dependence on hyperparameter tuning as, even though the integration of physical constraints through the PGNN improves the network's robustness, the effective- ness of the method still depends on the careful selection of hyperparameters, such as the weight coefficients for the physical loss function (α and β). (3) There are challenges with highly irregular interference as, in certain complex environments, such as those with severe

electromagnetic interference from nearby electronic equipment or geomagnetic anomalies, the performance of CEEMDAN-PGNN maybe limited. The model assumes that the magnetic interference is primarily generated by the aircraft, and, while it performs well under most conditions, it may struggle to handle extremely irregular interference that cannot be effectively decomposed by CEEMDAN. In future work, we will try the following improvements: (1) Real-time applications, future work could focus on optimizing the computational efficiency of CEEMDAN to enable real-time compensation, particularly for UAVs or autonomous systems operating in dynamic environments. (2) Generalization to complex environments could be conducted to further enhance the method's robustness, and future studies could explore its performance in more diverse and challenging environments, such as urban areas with high levels of electromagnetic interference or regions with significant geomagnetic anomalies. (3) Integration with other sensor modalities could be attempted as another promising direction is the fusion of aeromagnetic data with other sensor modalities [37]. This would allow for a more comprehensive understanding of the environment and enable more accurate detection and mapping of geological features or anomalies.

5. Conclusions

In this study, we demonstrated the effectiveness of the proposed compensation method under various conditions, including simulated, noisy, and real flight data. CEEMDAN- based decomposition would enhance the network's ability to handle complex interference, and integrating physical knowledge via PGNN would improve model stability and generalization in noisy environments. Our experiments confirm that CEEMDAN-PGNN outperforms traditional model-driven and data-driven methods in terms of compensation performance and robustness. Under simulated conditions, the proposed method reduced the interference in the original data from a standard deviation of 0.6998 nT to 0.02 nT, thus achieving an improvement ratio of 34.9877. When Gaussian and colored noise were introduced, the CEEMDAN-PGNN method consistently maintained a low residual error, whereas traditional methods such as LS and ridge regression exhibited significant performance degradation. In real flight tests, the compensation method reduced the magnetic interference amplitude from 6 nT to 0.1 nT, demonstrating its practical applicability. The improvement ratio achieved in actual flight data further underscores the method's strong potential for real-world use, where data quality can vary.

Acknowledgements

The authors acknowledge the National Natural Science Foundation of China (Grant: 61172017).

References

1. Gavazzi, B.; Le Maire, P.; deLépinay, J.M.; Calou, P.; Munschy, M. Fluxgate three-component magnetometers for cost-effective ground, UAV and airborne magnetic surveys for industrial and academic geoscience applications and comparison with current industrial standards through case studies. Geomechanics for Energy and the Environment **2019**, 20, 100117.
2. Dames, P.M.; Schwager, M.; Rus, D.; Kumar, V. Active magnetic anomaly detection using multiple micro aerial vehicles. IEEE Robotics and Automation Letters **2015**, 1, 153–160.
3. Mu, Y.; Chen, L.; Xiao, Y. Small Signal Magnetic Compensation Method for UAV-Borne Vector Magnetometer System. IEEE Transactions on Instrumentation and Measurement **2023**, 72, 1–7.
4. Xu, X.; Huang, L.; Liu, X.; Fang, G. Deepmad: Deep learning for magnetic anomaly detection and denoising. IEEE Access **2020**, 8, 121257–121266.
5. QIAO, Z.; MA, G.; ZHOU, W.; YU, P.; ZHOU, S.; WANG, T.; TANG, S.; DAI, W.; MENG, Z.; ZHANG, Z. Research on the comprehensive compensation of aeromagnetic system error of multi-rotor UAV. Chinese Journal of Geophysics **2020**, 63, 4604–4612.
6. Tolles, W.E.; Lawson,J. Magnetic compensation of MAD equipped aircraft. Airborne Instruments Lab. Inc., Mineola, NY, Rept **1950**, pp. 201–1.
7. Gnadt, A.R.; Wollaber, A.B.; Nielsen, A.P. Derivation and extensions of the tolles-lawson model for aeromagnetic compensation. arXiv preprint arXiv:2212.09899 2022.
8. Leliak, P. Identification and evaluation of magnetic-field sources of magnetic airborne detector equipped aircraft. IRE Transactions on Aerospace and Navigational Electronics **1961**, pp. 95–105.
9. Dou, Z.; Han,Q.; Niu, X.; Peng, X.; Guo, H. An aeromagnetic compensation coefficient-estimating method robust to geomagnetic gradient. IEEE Geoscience and Remote Sensing Letters **2016**, 13, 611–615.

10. Hardwick, C. Techniques for achieving stable and robust aeromagnetic compensation coefficients in 56th Ann. Internat. Mtg. Soc. of Expl. Geophys., Session: GM1 **1986**, 1.
11. Wu, P.; Zhang,Q.; Chen, L.; Zhu, W.; Fang, G. Aeromagnetic compensation algorithm based on principal component analysis. Journal of Sensors **2018**, 2018, 5798287.
12. Mengyin, F.; Jie, L.; Tailin, W.; Tong, L.; Meiling, W.; Kai, W.; Jiapeng, K. Aeromagnetic compensation based on Tikhonov regularization with limited L-curve parameter-choice algorithm. In Proceedings of the 2018 37th Chinese Control Conference (CCC). IEEE, 2018,pp. 1834–1838.
13. Zhao, G.; Han,Q.; Peng, X.; Zou, P.; Wang, H.; Du, C.; Wang, H.; Tong, X.; Li,Q.; Guo, H. An aeromagnetic compensation method based on a multimodel for mitigating multicollinearity. Sensors **2019**, 19, 2931.
14. Bi, F.; Yu, P.; Jiao,J.; Zhou, L.; Zeng, X.; Zhou, S. An adaptive modeling-based aeromagnetic maneuver noise suppression method and its application in mine detection. Remote Sensing **2023**, 15, 4590.
15. Ge, L.; Han,Q.; Qiao, Z.; Meng, Z. Innovative Aeromagnetic Compensation Techniques for In-Cabin Magnetometers Amidst Complex OBE Interference. IEEE Sensors Journal **2024**.
16. Wang, L.; Zheng,J.; Yang, F.; Xue, D.; Xiong, S. Research on Improving Small Signal Magnetic Compensation Method Based on Fixed Wing Unmanned Aerial Vehicle. IEEE Geoscience and Remote Sensing Letters **2024**.
17. Zhao, Y.; Jiao,J.; Huang, Y.; Yu, P.; Zhou, S.; Bi, F. Research on real-time compensation method of UAV aeromagnetic based on deep learning. In Proceedings of the International Workshop on Gravity, Electrical & Magnetic Methods and Their Applications, Shenzhen, China, May 19–22, 2024. Society of Exploration Geophysicists and Chinese Geophysical Society, 2024,pp. 314–318.
18. Williams, P.M. Aeromagnetic compensation using neural networks. Neural Computing & Applications **1993**, 1, 207–214.
19. Zhou, S.; Yang, C.; Su, Z.; Yu, P.; Jiao,J. An aeromagnetic compensation algorithm based on radial basis function artificial neural network. Applied Sciences **2022**, 13, 136.
20. Yu, P.; Bi, F.; Jiao,J.; Zhao, X.; Zhou, S.; Su, Z. An Aeromagnetic Compensation Algorithm Based on a Residual Neural Network. Applied Sciences **2022**, 12, 10759.
21. Zhang, D.; Liu, X.; Qu, X.; Zhu, W.; Huang, L.; Fang, G. Analysis of aeromagnetic swing noise and corresponding compensation method. IEEE Transactions on Geoscience and Remote Sensing **2021**, 60, 1–10.
22. Wang, Y.; Han,Q.; Zhan, D.; Li,Q. A data-driven OBE magnetic interference compensation method. Sensors **2022**, 22, 7732.
23. Karpatne, A.; Watkins, W.; Read,J.; Kumar, V. Physics-guided neural networks (pgnn): An application in lake temperature modeling. arXiv 2017. arXiv preprint arXiv:1710.11431 **2017**.
24. Wang,J.; Li, Y.; Zhao, R.; Gao, R.X. Physics guided neural network for machining tool wear prediction. Journal of Manufacturing Systems **2020**, 57, 298–310.
25. Bento, M.E. Physics-guided neural network for load margin assessment of power systems. IEEE Transactions on Power Systems **2023**, 39, 564–575.
26. Zhang, W.; Qu, Z.; Zhang, K.; Mao, W.; Ma, Y.; Fan, X. A combined model based on CEEMDAN and modified flower pollination algorithm for wind speed forecasting. Energy conversion and management **2017**, 136, 439–451.
27. Xu, Y.; Liu, Z.; Zhang, Q.; Liu, X.; Huang, B.; Pan, M.; Hu,J.; Chen, D.; Ying, T.; Qiu, X. Interference Model Guided Neural Network for Aeromagnetic Compensation. IEEE Sensors Journal **2024**.
28. Jiang, L.; Guo, Z.; Zhang, B. Scalar calibration of aeromagnetic data using BPANN and LS algorithms based on fixed-wing UAV platform. IEEE Transactions on Instrumentation and Measurement **2015**, 64, 1968–1976.
29. Gavazzi, B.; Le Maire, P.; deLépinay, J.M.; Calou, P.; Munschy, M. Fluxgate three-component magnetometers for cost-effective ground, UAV and airborne magnetic surveys for industrial and academic geoscience applications and comparison with current industrial standards through case studies. Geomechanics for Energy and the Environment **2019**, 20, 100117.
30. Forrester, R.; Huq, M.S.; Ahmadi, M.; Straznicky, P. Magnetic signature attenuation of an unmanned aircraft system for aeromagnetic survey. IEEE/ASME Transactions on Mechatronics **2013**, 19, 1436–1446.
31. Gnadt, A.R.; Wollaber, A.B.; Nielsen, A.P. Derivation and extensions of the tolles-lawson model for aeromagnetic compensation. arXiv preprint arXiv:2212.09899 **2022**.
32. Gnadt, A.R. Advanced aeromagnetic compensation models for airborne magnetic anomaly navigation; Massachusetts Institute of Technology, 2022.

33. Mengyin, F.; Jie, L.; Tailin, W.; Tong, L.; Meiling, W.; Kai, W.; Jiapeng, K. Aeromagnetic compensation based on Tikhonov regularization with limited L-curve parameter-choice algorithm. In Proceedings of the 2018 37th Chinese Control Conference (CCC). IEEE, 2018,pp. 1834–1838.
34. Zheng, Y.; Li, S.; Xing, K.; Zhang, X. A novel noise reduction method of UAV magnetic survey data based on CEEMDAN, permutation entropy, correlation coefficient and wavelet threshold denoising. Entropy **2021**, 23, 1309.
35. Noriega, G. Performance measures in aeromagnetic compensation. The Leading Edge **2011**, 30, 1122–1127.
36. Noriega, G. Aeromagnetic compensation ingradiometry—Performance, model stability, and robustness. IEEE Geoscience and Remote Sensing Letters **2014**, 12, 117–121.
37. Park, S.; Oh, S. Enhanced and multi-purpose analysis of aeromagnetic anomalies supported by topographic data. Environmental Earth Sciences **2024**, 83, 595.